Wave-function reconstruction of complex fields obeying nonlinear parabolic equations

Yaw-Ren E. Tan, David M. Paganin, Rotha P. Yu, and Michael J. Morgan
School of Physics and Materials Engineering, Monash University, Victoria 3800, Australia
(Received 25 June 2003; published 11 December 2003)

We present a generalized Gerchberg-Saxton (GS) algorithm for reconstructing a (2+1)-dimensional complex scalar wave field which obeys a known nonlinear nondissipative parabolic differential equation, given knowledge of the wave-field modulus at three or more values of an evolution parameter such as time. This algorithm is used to recover the complex wave function of a (2+1)-dimensional Bose-Einstein condensate (BEC) from simulated modulus data. The Gross-Pitaveskii equation is used to model the dynamics of the BEC, with the modulus information being provided by a temporal sequence of simulated absorption images of the condensate. The efficacy of the generalized GS algorithm is examined for a wide range of simulation conditions, including strong nonlinearities, vortex states and Poisson noise. The general form of this algorithm, which allows one to reconstruct a time-dependent wave function, will be useful for studying the phase dynamics of topological defects in coherent quantum systems.

DOI: 10.1103/PhysRevE.68.066602 PACS number(s): 42.30.Rx, 03.75.Lm, 03.75.Kk

I. INTRODUCTION

The celebrated ''phase problem'' poses the question of determining the phase of a complex function using information about its modulus, supplemented by any relevant *a priori* knowledge. Solutions to particular phase problems (i.e., phase retrieval) have been studied in fields as diverse as astronomical imaging [1], crystallography [2], optical microscopy [3], electron microscopy [4], point projection imaging [5], and x-ray diffraction [6]. These examples deal with the problem of phase retrieval for matter or radiation wave fields whose evolution is governed by linear partial differential equations. However, not all systems are governed by linear equations. For example, nonlinear electromagnetic wave phenomena such as solitons [7] have long been studied by the nonlinear optics community. Nonlinear evolution also occurs for water waves [8], acoustic waves [9], and plasmas [10]. A topical example of nonlinear wave-field evolution is Bose-Einstein condensation, the dynamics of which are modeled at zero temperature by a nonlinear parabolic partial differential equation for the complex order parameter—the Gross-Pitaevskii equation [11–13].

There is emerging interest in the problem of phase retrieval for wave fields which obey nonlinear equations (see, e.g., Ref. [14,15]). Such studies have made first steps towards the goal of routinely determining phase for strongly nonlinear systems. An important motivation for these studies is the fact that the canonical method of phase reconstruction, namely, interferometry [16], is not applicable to strongly nonlinear systems. Interferometric phase determination fails because the superposition principle does not hold for nonlinear wave fields: the superposition of the ''reference wave'' and the wave field under study is not a valid solution to a given nonlinear equation, even if the two wave fields separately satisfy this equation.

The aim of this paper is to derive a phase-retrieval method, applicable to nonlinear complex fields, which generalizes the Gerchberg-Saxton (GS) algorithm [17]. This is applied to the reconstruction of complex wave fields that obey known (2+1)-dimensional nondissipative nonlinear parabolic partial differential equations, given as data the modulus of the wave field at three or more values of a given evolution parameter. This evolution parameter is typically either time t or propagation distance z; we refer to the evolution parameter as ''time'' for the remainder of the paper. Solution to a given phase problem amounts to obtaining total knowledge of a quantum-mechanical complex wave field (as encoded in the complex scalar wave function, macroscopic wave function, or order parameter), or of a classical scalar radiation wave field (as encoded in its complex analytic signal [16]), given as data the modulus of the wave over certain surfaces in space time. We will refer to such modulus data as ''holographic snapshots,'' since they constitute in-line holograms in the sense originally formulated by Gabor [18].

The outline of the paper is as follows. In Sec. II we describe the algorithm for the phase retrieval of waves obeying known nonlinear parabolic equations, given a set of holographic snapshots. These snapshots may be supplemented by any relevant *a priori* knowledge which places constraints on the value of the wave function on the surfaces over which the holographic snapshots are taken. This algorithm is a generalization of the famous method of phase retrieval due to Gerchberg and Saxton [17,19]. As an example of the application of these ideas to a strongly nonlinear vortex-riddled system, Sec. III gives a robust means for recovering the wave function of a (2+1)-dimensional Bose-Einstein condensate which evolves according to the Gross-Pitaevskii equation, given simulated images of the modulus of the wave function at three or more times. We highlight the efficacy of the algorithm and discuss its applicability to experimental observations. We offer a discussion in Sec. IV, and conclude with Sec. V.

II. GENERALIZED GERCHBERG-SAXTON ALGORITHM

The Gerchberg-Saxton (GS) algorithm [17,19] is a well-known solution to the following phase problem: given the modulus $|\Psi(\mathbf{r}_\perp)|$ of a complex scalar function of two space variables $\mathbf{r}_\perp \equiv (x,y)$, together with the modulus $|\hat{F}\{\Psi(\mathbf{r}_\perp)\}|$ of its Fourier transform with respect to $\mathbf{r}_\perp$, can one reconstruct the complex wave function $\Psi(\mathbf{r}_\perp)$? This phase problem, now known as the ''Pauli problem,'' was first consid-

ered by Pauli in the context of quantum mechanics [20].

In its original and simplest form [17], the Gerchberg-Saxton algorithm claims the following iterative solution to the Pauli problem:

$$\Psi(\mathbf{r}_\perp) = \lim_{N\to\infty} (\hat{P}_1 \hat{F}^{-1} \hat{P}_2 \hat{F})^N |\Psi(\mathbf{r}_\perp)|. \tag{1}$$

Here, N is the number of iterations of the algorithm (taken to be sufficiently large for convergence to be attained), $\hat{F}$ denotes the operator for Fourier transformation with respect to $\mathbf{r}_\perp$, $\hat{F}^{-1}$ is the inverse Fourier transform, $\hat{P}_1$ is a projection operator which replaces the modulus of the function on which it acts by the known function $|\Psi(\mathbf{r}_\perp)|$, and $\hat{P}_2$ is a projection operator which replaces the modulus of the function on which it acts by the known function $|\hat{F}\Psi(\mathbf{r}_\perp)|$. Note that all operators in Eq. (1) act from right to left on the initial estimate $|\Psi(\mathbf{r}_\perp)|$ for the reconstructed wave function, which has the correct modulus and a constant phase.

Convergence of this algorithm is often problematic, with stagnation being a common problem [21]. Modifications such as those due to Fienup [21] may be used to achieve a more robust algorithm for attacking a given Pauli problem, although one might argue that such modifications lack the compelling simplicity of Gerchberg and Saxton's original proposal. For recent work employing the Gerchberg-Saxton-Fienup algorithm, see Weierstall *et al.* [22] and references therein.

In this article, we do not follow Fienup and others in seeking modified forms of the Gerchberg-Saxton algorithm which better solve the Pauli problem. Rather, we turn our attention to a class of related but different phase problems, which make use of slightly larger datasets of three or more images. With this in mind, note that the Fourier transform operator, which appears in Eq. (1), is unitary. This unitary operator may be replaced by a different unitary operator [23], such as the Fresnel transform [24] (which evolves a solution to the linear parabolic equation forwards or backwards in time); note that the Fresnel transform is formally identical to the time evolution operator for the (2+1)-dimensional free-space time-dependent Schrödinger equation. One is therefore led to a variant of the GS algorithm using a sequence of two-dimensional images related to one another by the Fresnel transform [25]. Superior results may be obtained when more than two images are incorporated into this algorithm [26]. In particular, Allen *et al.* [27,28] used a through focal series (TFS) $\{|\Psi(\mathbf{r}_\perp,t_1)|, |\Psi(\mathbf{r}_\perp,t_2)|, |\Psi(\mathbf{r}_\perp,t_3)|, \cdots\}$ of three or more images to demonstrate the robustness of the GS algorithm in the presence of both noise and vortices; they did this for the case of a wave function obeying the linear Schrödinger equation

$$(i\alpha\partial/\partial t + \nabla_\perp^2)\Psi(\mathbf{r}_\perp,t) = 0, \tag{2}$$

where α is a constant, $\nabla_\perp^2$ is the Laplacian in the two-dimensional plane containing $\mathbf{r}_\perp$, and t is the propagation distance for a time-independent paraxial beam along a nominal optic axis [29]. When three images were employed, application of a modified GS algorithm with Fourier transforms replaced by Fresnel transforms, namely

$$\Psi(\mathbf{r}_\perp,t_1) = \lim_{N\to\infty} (\hat{P}_1 \hat{U}_{2,1} \hat{P}_2 \hat{U}_{3,2} \hat{P}_3 \hat{U}_{2,3} \hat{P}_2 \hat{U}_{1,2})^N |\Psi(\mathbf{r}_\perp,t_1)|, \tag{3}$$

yielded extremely robust and stagnation-free convergence to the correct solution for a wide variety of numerical experiments. Here, the Fresnel transform $\hat{U}_{m,n}$ (time-evolution operator) for Eq. (2) is defined by $\hat{U}_{m,n}\Psi(\mathbf{r}_\perp,t_m) = \Psi(\mathbf{r}_\perp,t_n)$, where $m,n=1,2,3$, and $\hat{P}_m$ is a projection operator which replaces the modulus of the function on which it acts by the known function $|\Psi(\mathbf{r}_\perp,t_m)|$. The robustness of this algorithm, when applied to three or more images, was maintained even in the presence of spontaneously-generated wave field vortices.

Both Eqs. (1) and (3) apply an iterated sequence of operators (projection operator, unitary operator, projection operator, unitary operator *etc.*) to an initial estimate for the reconstructed wave function which has the correct modulus and a constant phase. The three images employed in Eq. (3) were found to lead to considerably greater robustness in numerical experiments when compared to reconstructions based on two images. This robustness was maintained when the Fresnel transform in Eq. (3) was replaced with a more general class of linear unitary operators describing coherent shift-invariant linear imaging systems [30].

In the context of the present paper, we explore generalized forms of Eq. (3) which replace $\hat{U}$ with a unitary nonlinear evolution operator. Consider the following class of nonlinear nondissipative parabolic equations (cf. Ref. [15])

$$(i\alpha\partial/\partial t + \gamma\nabla_\perp^2 + \beta + V + f(|\Psi|))\Psi = 0, \tag{4}$$

where α,β,γ are real numbers, $V \equiv V(\mathbf{r}_\perp,t)$ is a real potential, f is a real function of a real variable, and $\Psi \equiv \Psi(\mathbf{r}_\perp,t)$ is a complex function of two space variables $\mathbf{r}_\perp \equiv (x,y)$ and one evolution parameter t. Special cases of our class of nondissipative nonlinear equations include the (2+1)-dimensional linear and nonlinear Schrödinger equations [31], the paraxial equation of classical scalar optics [29], the (2+1)-dimensional Gross-Pitaevskii equation [11–13], and the cubic-quintic parabolic equation for "liquid light" [32].

We address the following nonlinear phase problem: Given a consecutive series $\{|\Psi(\mathbf{r}_\perp,t_1)|, |\Psi(\mathbf{r}_\perp,t_2)|, \ldots, |\Psi(\mathbf{r}_\perp,t_M)|\}$ of $M \geqslant 3$ holographic snapshots, where $\Psi(\mathbf{r}_\perp,t)$ obeys a known equation which is a special case of Eq. (4), can we reconstruct the full complex wave function $\Psi(\mathbf{r}_\perp,t)$? The wave function is to be reconstructed for all times lying in the time interval $t \in (t_1-\Delta_1, t_M+\Delta_2)$, where the positive real numbers Δ_1 and Δ_2 are sufficiently small that, at the numerical accuracy to which the wave function is approximated and the modulus data measured, the value of the wave function for any $t \in (t_1-\Delta_1, t_1)$ or $t \in (t_M, t_M+\Delta_2)$ may be accurately obtained from the boundary values $\Psi(\mathbf{r}_\perp,t_1)$ and $\Psi(\mathbf{r}_\perp,t_M)$, respectively. Similarly $|t_m - t_{m+1}|$, where $m=1,2,\ldots,M-1$, must be sufficiently small that, at the numerical accuracy to which the wave func-

tion is approximated and the modulus data measured, $\Psi(\mathbf{r}_\perp,t)$ for any $t\in(t_m,t_{m+1})$ may be accurately obtained from either of the respective boundary values $\Psi(\mathbf{r}_\perp,t_m)$ or $\Psi(\mathbf{r}_\perp,t_{m+1})$.

We postulate that the following generalized Gerchberg-Saxton (GGS) algorithm gives a solution to our nonlinear phase problem (cf. Ref. [30]):

$$\Psi(\mathbf{r}_\perp,t_1)=\lim_{N\to\infty}\left(\prod_{i=1}^{M-1}\hat{P}_i'\hat{U}_{i+1,i}\prod_{i=M}^{2}\hat{P}_i'\hat{U}_{i-1,i}\right)^N|\Psi(\mathbf{r}_\perp,t_1)|. \tag{5}$$

Since the class of Eqs. (4) is nondissipative, the associated nonlinear time evolution operator $\hat{U}$ will be unitary: we define this operator via the equation $\hat{U}_{m,n}\Psi(\mathbf{r}_\perp,t_m)=\Psi(\mathbf{r}_\perp,t_n)$, with $\hat{U}$ being such that Ψ is a solution to Eq. (4). If no *a priori* knowledge is assumed, then $\hat{P}_m'=\hat{P}_m$. If, however, additional constraints on any or each of the wave functions $\Psi(\mathbf{r}_\perp,t_m)$ are given, then $\hat{P}_m'=\hat{P}_m''\hat{P}_m$, where $\hat{P}_m''$ is an operator which projects the wave function upon which it acts into the space of wave functions consistent with the given *a priori* knowledge. For example, $\hat{P}_m''$ might be used to impose such *a priori* knowledge as finite support for a given value of t.

Equation (5) contains as special cases the GS algorithm [17] of Eq. (1), Misell's algorithm [25], the TFS algorithm of Eq. (3), and variations of the TFS used in Ref. [30]. This algorithm retains the compelling simplicity of Gerchberg and Saxton's original proposal, as Eqs. (1) and (5) both comprise an iterated sequence of unitary evolution and projection operators, which is applied to an initial estimate of the reconstructed wave function that has the correct modulus and a constant phase.

III. RECOVERING THE WAVE FUNCTION OF A BOSE-EINSTEIN CONDENSATE

Bose-Einstein condensates [33,34] give an interesting arena for retrieving the phase distribution of a wave function whose underlying dynamics are nonlinear. Such condensates provide the opportunity to engineer a complex-valued macroscopic wave function (order parameter). For example, rotating a Bose-Einstein condensate (BEC) gives rise to quantized vortices [35,36] which can be observed using absorption or dispersive imaging techniques [37]. In this context, phase retrieval gives a useful tool for studying the dynamics of topological phase defects [38]. In this section, we apply a special case of Eq. (5) to the problem of reconstructing the wave function of a (2+1)-dimensional Bose-Einstein condensate.

A. Modeling of a (2+1)-dimensional BEC

To simulate a BEC we employ a mean-field approach using the Gross-Pitaevskii (GP) equation [11–13], neglecting quantum and thermal fluctuations. We assume confinement of the BEC in the z direction, which allows us to describe the condensate in the two-dimensional transverse plane $\mathbf{r}_\perp\equiv(x,y)$. The simulated BEC is confined in a trap modeled by a harmonic oscillator potential [39]

$$V_{trap}(\mathbf{r}_\perp)=\tfrac{1}{2}m\omega^2r_\perp^2, \tag{6}$$

where m is the mass of the atomic species $r_\perp^2\equiv|\mathbf{r}_\perp|^2$, and ω_x,ω_y are oscillator frequencies which determine the trap frequency via $\omega=\sqrt{\omega_x^2+\omega_y^2}$. We now introduce dimensionless harmonic oscillator units [40] in which the unit of length a_{ho} corresponds to the average width of the Gaussian ground-state wave function: $a_{ho}=\sqrt{\hbar/(m\omega_{ho})}$, where $\omega_{ho}=\sqrt{\omega_x\omega_y}$ is the geometric mean of the oscillator frequencies. Using rescaled variables for which ω_{ho}^{-1}, a_{ho}, and $\hbar\omega_{ho}$ are the units of time, length, and energy, respectively, the time-dependent GP equation may be written as

$$i\frac{\partial}{\partial t}\Psi=[-\tfrac{1}{2}\nabla_\perp^2+\tfrac{1}{2}r_\perp^2+V(|\Psi|)]\Psi, \tag{7}$$

where $\Psi\equiv\Psi(\mathbf{r}_\perp,t)$ is the condensate wave function normalized to unity, and $\nabla_\perp^2$ is the Laplacian in the x-y plane. We identify the nonlinear term $V(|\Psi|)=g|\Psi|^2$ with atomic interactions in the Bose gas, where g is the coupling constant (self-interaction coefficient). This constant is related to the s-wave scattering length a_s of a binary collision by $g=4\pi Na_s/a_{ho}$, where N is the number of atoms in the condensate [40].

To simulate the BEC, Eq. (7) was evolved through time using a fourth order Runge-Kutta method with spatial step $\Delta h=0.15$ and time step $\Delta t=0.003$. These parameters were chosen to ensure stability of the numerical integration scheme, and were used for all simulations in this paper. In these simulations, the initial condition used was the ground state wave function of the condensate in the given trapping potential. This ground state was calculated by using the time-independent GP equation that follows from substituting $\Psi(\mathbf{r}_\perp,t)=\Psi(\mathbf{r}_\perp)e^{-i\mu t}$ into Eq. (7), where μ is a real energy parameter (chemical potential). The time-independent GP equation is then given by

$$\mu\Psi(\mathbf{r}_\perp)=[-\tfrac{1}{2}\nabla_\perp^2+\tfrac{1}{2}r_\perp^2+g|\Psi(\mathbf{r}_\perp)|^2]\Psi(\mathbf{r}_\perp). \tag{8}$$

Equation (8) was solved for the ground-state wave function using a diffusion Monte Carlo method [41], which finds the minimum energy configuration using a steepest descent approach. In the absence of interactions ($g=0$), Eq. (8) reduces to that for the quantum harmonic oscillator, whose ground state is a Gaussian wave function. However, for $g>0$ the condensate is broadened relative to the $g=0$ case, as a result of repulsive atomic interactions.

B. Absorption imaging of a BEC

BECs can be imaged using absorption, fluorescence, and dispersive techniques [39]. We shall consider simulated absorption images as input to the GGS algorithm in Eq. (5). However, we emphasize that dispersive imaging is equally well suited to the phase-retrieval methodology described

here, provided that one is able to use a dispersive image to compute the probability density which forms the input to the GGS algorithm [37].

Here, we assume a thin lens approximation and consider the case where coherent laser probe light, propagating in the z direction, arrives perpendicular to the x-y plane containing the condensate. The probe light field is assumed to be uniform immediately upstream of this plane, and the condensate is assumed to be well approximated by two-level atoms under the rotating-wave approximation. The intensity of the probe light at the exit surface of the BEC is then [39]

$$I(\mathbf{r}_\perp) = I_0 \exp\left(-\frac{\sigma_0 \tilde{n}}{1+\delta^2} \right), \tag{9}$$

where I_0 is the incident intensity of the probe beam, σ_0 is the resonant scattering cross section, $\tilde{n} \equiv \int n(\mathbf{r}_\perp, z)dz$ is the integrated number density of atoms in the condensate, and δ is the detuning factor measured in half linewidths of the probe laser. This detuning factor is defined as $\delta = (\omega - \omega_0)/((1/2)\Gamma)$, where ω_0 is the resonant frequency of the BEC, ω is the frequency of the probe light, and Γ is the linewidth of the laser. Note that we identify $\tilde{n}(\mathbf{r}_\perp, t)$ with $N|\Psi(\mathbf{r}_\perp, t)|^2$.

In all simulations presented in this paper, Eq. (9) was used to model the process of forming an absorption image. Before being used as input into Eq. (5), each series of simulated absorption images was digitized to 16 bits. This was achieved by adjusting the detuning parameter δ, which appears in the normalized absorption coefficient $\sigma_0/(1+\delta^2)$, to ensure that the range of digitized transmitted intensity signals lies within the range 500–65 000 counts.

C. Case I—Interference of two BECs

We first consider the situation where two spatially separated BECs are created in a double-well trapping potential, and then allowed to expand and overlap after the trap is turned off [42] (''Case I''). This double well potential was modeled by replacing the trap potential $(1/2)r_\perp^2$ in Eq. (7) with $(1/2)r_\perp^2 + V_{laser}$, where V_{laser} is the potential associated with a thin static sheet of laser light bisecting the trap. We modeled the potential of this sheet with the Gaussian

$$V_{laser} = \alpha \exp[-\beta_x (x-x_0)^2 - \beta_y (y-y_0)^2], \tag{10}$$

where $\alpha = 100$ is the peak value of the potential, $\beta_x = 0.306$ and $\beta_y = 0.010$ are inversely proportional to the width of the laser beam in the x and y directions, and $(x_0, y_0) = (0,0)$ gives the centroid of the beam.

In this and all subsequent simulations, the Cartesian coordinate system (x,y) is mapped onto a square lattice of $2^m \times 2^m$ pixels, where m is a positive integer. The origin $(x,y) = (0,0)$ of Cartesian coordinates is identified with the ''central'' pixel, whose location is reached by first moving $2^{m-1} - 1$ pixels to the right of the bottom-left pixel, and then moving $2^{m-1} - 1$ pixels above the resulting lattice point. The physical width and height of each pixel was, in all simulations, equal to the spatial step $\Delta h = 0.15$; the time step was in all cases equal to $\Delta t = 0.003$.

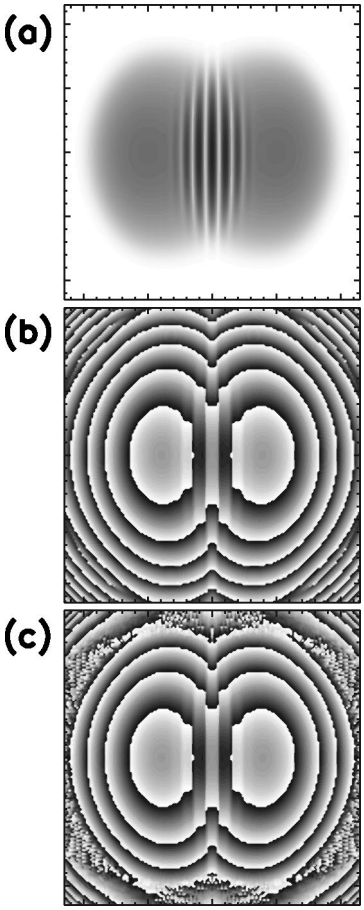

FIG. 1. Grayscale plots of (a) simulated modulus and (b) phase of two overlapping BECs, 300 time steps after a double-well trap has been turned off and the condensate allowed to expand ($g = 1000$). (c) Phase retrieved with $N = 300$ iterations of Eq. (5), using as input data the five simulated absorption images at $t = 100$, 150, 200, 250, and 300 time steps after the trap was turned off. In all phase maps, which are modulo 2π, black denotes a phase of 0 and white denotes 2π.

Using the double-well potential $(1/2)r_\perp^2 + V_{laser}$, and $2^m = 256$ pixels, the BEC was modeled with three different self-interaction coefficients: $g = 0$, $g = 100$, and $g = 1000$. The latter two values for g correspond to a high degree of nonlinearity. The initial condition (ground state) of the BEC was generated for each value of g using the procedure described in Sec. III A. Figs. 1(a) and 1(b) show the modulus and phase of the $g = 1000$ case of the interference of two spatially separated BECs, respectively, $t = 300$ time steps after the trap has been switched off, allowing the BEC pair to expand and overlap. Note that Fig. 1(c) will be discussed in Sec. III E.

D. Case II—Stirred condensate

We next consider stirring a BEC with a tightly focused blue-detuned laser beam [43,44] (''Case II''). This blue-detuned laser light was modeled by a moving Gaussian potential

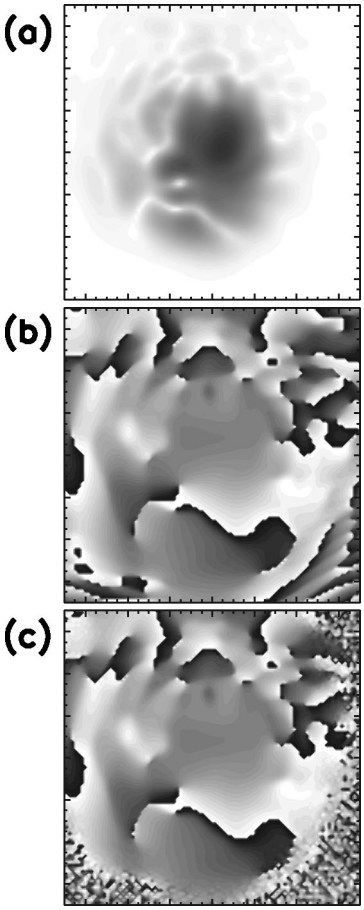

FIG. 2. Grayscale plots of (a) modulus and (b) phase of a simulated BEC, 4600 time steps after completing stirring of the ground state of a harmonic trap with a moving laser spot ($g=100$). (c) Phase retrieved with $N=20$ iterations of Eq. (5), using as input data the nine simulated absorption images at $t=3800$, 3900, 4000, 4100, 4200, 4300, 4400, 4500, and 4600 time steps after stirring was commenced. In all phase maps, which are modulo 2π, black denotes a phase of 0 and white denotes 2π.

$$V_{laser}=\alpha\ \exp[-\beta_x(x-x_0-v_xt)^2-\beta_y(y-y_0-v_yt)^2]. \tag{11}$$

The centroid of this potential has initial coordinates (x_0,y_0), with this centroid being swept through the condensate with velocity (v_x,v_y). The Gaussian potential of the moving laser beam was again incorporated into the GP equation (7) by using the potential $(1/2)r_\perp^2+V_{laser}$. The parameters used in Eq. (11) were $\alpha=30$, $\beta_x=\beta_y=3$, $(x_0,y_0)=(-1,-11)$, $(v_x,v_y)=(0,2)$. The ground-state initial condition was generated over a 128×128 pixel grid without the laser beam, with $g=100$. We then ''switched on'' the moving laser potential at $t=0$. The parameters chosen for the potential in Eq. (11) are such that the stirring laser beam, which is initially outside the simulation frame, is passed through the condensate before leaving the simulation frame at $t=2900$ timesteps. Figures 2(a) and 2(b) show the modulus and phase of the condensate wave function, respectively, 4600 time steps after the stirring was completed. A number of counterpropagating quantized vortex pairs have been nucleated by the laser stirring, these being evident as screw dislocations in the multivalued phase [38] of the wave function in Fig. 2(b). Figure 2(c) will be discussed in the following section.

E. Phase Retrieval of the BEC Wave function

Here, we model the phase retrieval of a BEC wave function using Eq. (5), in which the nonlinear unitary time evolution operator $\hat{U}$ is determined by Eq. (7). The input to the GGS algorithm in Eq. (5) is obtained from three or more sequential absorption images of the BEC. To synthesize these absorption images the condensate is modeled according to either Case I or II, allowed to evolve for a fixed time, and then imaged according to Eq. (9). The natural logarithm of each of these absorption images is proportional to the modulus of the condensate wave function.

Since the condensate is disturbed by the absorptive imaging process, experimental recording of the multiple images used in Eq. (5) requires identical systems to be prepared and evolved for different times before being imaged. In this way it is possible to record the dynamics of an evolving BEC [45], and hence obtain the necessary data for wave function reconstruction using Eq. (5). Alternatively, one may use quantitative dispersive imaging techniques such as those described by Turner *et al.* [37] to nondestructively obtain such a series of images using a single condensate.

Figure 1 shows the phase reconstruction for the nonlinear double-well simulation described in Sec. III C. Here a sequence of five images, at $t=100$,150,200,250, and 300 time steps after switching off the double-well trap, was used as input for Eq. (5). This noise-free simulation required 300 iterations of Eq. (5) to yield the reconstructed phase at $t=300$, as shown in Fig. 1(c). Since the retrieved phase is only known up to an additive constant, the phase of both the true and reconstructed wave functions have been set to π at the central pixel.

Qualitatively, the phase in Fig. 1(c) is well reconstructed over all parts of the image for which the probability density is non-negligible. However, to give a quantitative measure of the closeness of the kth iterate $\tilde{\Psi}^{(k)}$ of the reconstructed wave function to the true wave function Ψ, we calculate the normalized root-mean-square (RMS) error by

$$\sigma_\Psi^{(k)}=\sqrt{\frac{\sum_{i=0}^{2^m-1}\sum_{j=0}^{2^m-1}|\Psi_{ij}(t)-\tilde{\Psi}_{ij}^{(k)}(t)|^2}{\sum_{i=0}^{2^m-1}\sum_{j=0}^{2^m-1}|\Psi_{ij}(t)|^2}}, \tag{12}$$

where i,j denote the grid coordinates in the $2^m\times2^m$ pixel image. Using this error metric, the RMS error in the wave function reconstruction of Fig. 1 is 2.7×10^{-3}. Having completed the $g=1000$ ''Case I'' reconstruction, the analysis was repeated for two further values of g, namely, $g=0$ and $g=100$. The $g=0$ version of Case I, with three images at $t=400$, 600, and 800 time steps after switching off the trap, required 498 iterations to yield a RMS reconstruction error of 6.9×10^{-3}. The $g=100$ version of Case I, with five im-

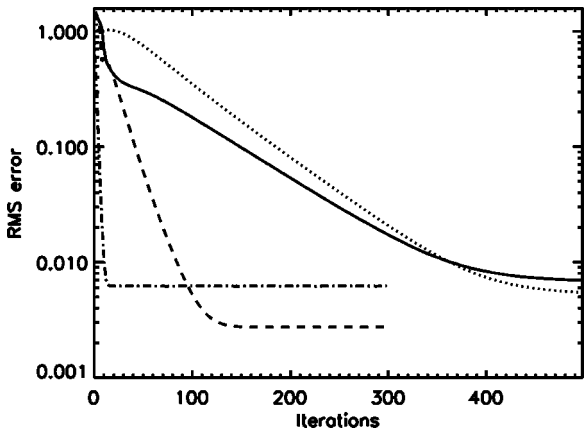

FIG. 3. RMS error $\sigma_\Psi^{(k)}$ in wave function reconstruction, calculated using Eq. (12), vs iteration number k. Case I, $g=0$ (solid line); Case I, $g=100$ (dotted line); Case I, $g=1000$ (dashed line); Case II, $g=100$ (dot-dashed line).

ages at $t=400,500,600,700$, and 800 time steps, required 498 iterations to yield a RMS reconstruction error of 5.5×10^{-3}. All of these RMS reconstruction errors compare favorably with the RMS error of approximately $1/\sqrt{2^{16}}\approx4\times10^{-3}$ which was introduced by the 16-bit digitization of the simulated absorption images, as described at the end of Sec. III B.

Figure 2 shows the phase reconstruction for the stirred BEC (''Case II'') in the presence of multiple vortices created using the procedure described in Sec. III D. A sequence of nine images, at $t=3800$, 3900, 4000, 4100, 4200, 4300, 4400, 4500, and 4600 time steps after commencing the stirring, was used as input for Eq. (5). This noise-free simulation required 20 iterations of Eq. (5) to yield the reconstructed phase at $t=4600$ time steps, as shown in Fig. 2(c). The phase of both the true and reconstructed wave functions was set to π at the central pixel. Using the error metric in Eq. (12), the error in the wave function reconstruction of Fig. 2 is 6.2×10^{-3}. Again, this compares favorably to the RMS error in the input data.

To give more insight into the convergence properties of wave function reconstruction using Eq. (5), Fig. 3 plots the RMS error $\sigma_\Psi^{(k)}$ versus iteration number k for the four scenarios described previously (i.e., Case I with $g=0,100,1000$ and Case II with $g=100$). We see that, in all cases, the RMS error exponentially approaches a value comparable to the RMS error ($\approx4\times10^{-3}$) which was introduced into the input data by the 16-bit digitization of the simulated absorption images. Interestingly, the case with multiple vortices has a significantly more rapid convergence than the three vortex-free cases. Of the vortex-free cases, it was the most strongly nonlinear ($g=1000$) that had the most rapid convergence.

Since the act of imaging a BEC perturbs the condensate, it is preferable to use as few probe photons as possible in forming an image of this quantum state: too many absorbed photons will destroy the condensate. In this context, we investigate the performance of Eq. (5) in the presence of significant

TABLE I. RMS error $\sigma_\Psi^{(k)}$ of the wave function reconstruction in the presence of noise. The error was measured after k iterations, at which point the algorithm had converged. All simulations, with the exception of those indicated with an asterisk, were vortex free.

g	ξ	σ_ξ	k	$\sigma_\Psi^{(k)}$
0	0.028	0.32	498	0.38
100	0.028	0.22	498	0.30
1000	0.028	0.19	200	0.21
100*	0.028	0.21	20	0.25

amounts of noise in the simulated absorption-contrast images. This noise was added by taking the noise-free 16-bit absorption images described in Sec. III B, and then replacing the intensity at each pixel with a random number drawn from a Poisson distribution; this distribution had a mean given by the noise-free photon count at each particular pixel, with the photon count being proportional to the noise-free signal in each pixel. The noise added to a given image is fixed once and for all by specifying the RMS Poisson noise ξ on the the maximum intensity of the noise-free image; this corresponds to a ray of the laser probe beam which does not pass through the condensate. Evidently, the RMS noise level σ_ξ in the absorption image will be greater (possibly much greater) than ξ. Table I summarizes the RMS error $\sigma_\Psi^{(k)}$ in the reconstruction, with $\xi=2.8\times10^{-2}$, for the four scenarios investigated in this paper (i.e., Case I with $g=0,100,1000$ and Case II with $g=100$). All of these RMS errors compare favorably with the RMS error σ_ξ introduced in simulating each of the noisy absorption images, with a maximum ''noise amplification factor'' of $\sigma_\Psi^{(k)}/\sigma_\xi\approx1.36$.

We close this series of simulations by studying the influence, upon the rate of convergence of the wave function reconstruction, of changing both (i) the number of images used, and (ii) the number of time steps allowed to elapse between consecutive images. For this final numerical study, we work with Case I using $g=1000$. The numerical results are shown in Fig. 4. We see that the algorithm converges exponentially rapidly to the ''noise floor'' for five out of the six studies presented there. We also note, from Fig. 4, that the algorithm's exponential rate of convergence is increased when one increases the number of images, while keeping constant the number of time steps between each of these images. Convergence was not achieved for the study which had both the largest number of time steps between images and the smallest number of images (three images, 100 time steps in between). For this nonconvergent case, keeping the number of images fixed while decreasing the number of time steps between images (from 100 to 50) led to convergence.

Why did the algorithm fail to converge when the number of time steps between images were too large? This is a manifestation of the well-known ''finite memory'' of nonlinear systems: sensitive dependence on initial conditions implies that too great an elapsed time, between a pair of finite-precision numerically evolved wave functions, precludes accurately tracing a direct causal link between the two. The presence of positive Lyapunov exponents in a volume-preserving phase-space flow implies that the ball of initial conditions, each consistent with the finite precision to which

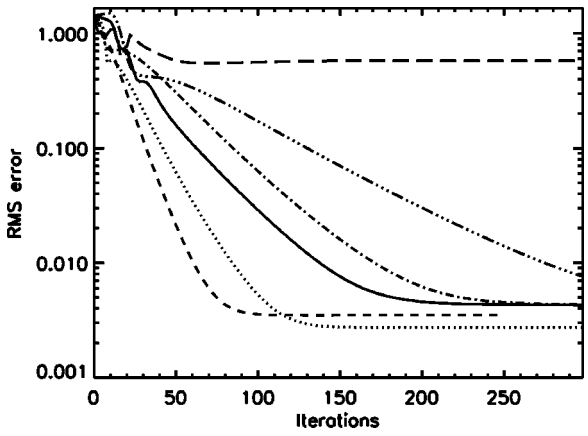

FIG. 4. RMS error $\sigma_{\Psi}^{(k)}$ of the reconstructed wave function as a function of iteration number k. The different lines represent different retrieval parameters for Case I with $g=1000$, using: three images with 100 time steps between images (long dash); five images with 25 time steps between images (dash ellipsis); nine images with 25 time steps (dash dot); three images with 50 time steps (solid line); five images with 50 time steps (dotted line); nine images with 50 time steps (short dash). In all cases, the first image corresponded to $t=100$ time steps after turning off the double-well trap.

the wave function is specified, will be folded/mixed through the accessible phase space during the flow governed by the nonlinear evolution equation [46]. Too great an evolution time between holographic snapshots will therefore imply that the reconstruction fails, since in evolving from snapshot to snapshot the result of applying the time-evolution operator is strongly perturbed by fluctuations below the noise level of the system.

IV. DISCUSSION

A. Wave function movies

The algorithm of Eq. (5) reconstructs the wave function $\Psi(\mathbf{r}_\perp,t_1)$ corresponding to time t_1, given the moduli of the wave function at all times in the ordered set $\{t_1,t_2,\cdots,t_M\}$. Having obtained $\Psi(\mathbf{r}_\perp,t_1)$, one can obtain $\Psi(\mathbf{r}_\perp,t_2)$ via $\Psi(\mathbf{r}_\perp,t_2)=\hat{P}_2\hat{U}_{1,2}\Psi(\mathbf{r}_\perp,t_1)$, a procedure that can be recursively applied to give

$$\Psi(\mathbf{r}_\perp,t_j)=\prod_{i=j-1}^{1}(\hat{P}_{i+1}\hat{U}_{i,i+1})\Psi(\mathbf{r}_\perp,t_1),2\leqslant j\leqslant M. \tag{13}$$

One therefore reconstructs the ordered wave function sequence $\Psi(\mathbf{r}_\perp,t_j)$, $j=1,\cdots,M$ corresponding to all times in the set $\{t_1,t_2,\cdots,t_M\}$. Moreover, one may also obtain a wave function "movie" by reconstructing the said wave function at any number of times t lying in the continuum $t\in(t_1-\Delta_1,t_M+\Delta_2)$ (see Sec. II). To reconstruct the wave function $\Psi(\mathbf{r}_\perp,t_{i'})$ at any given time $t_{i'}\in(t_1-\Delta_1,t_M+\Delta_2)$, first choose a member $t_{i''}$ of $\{t_1,t_2,\cdots,t_M\}$, which minimizes $|t_{i'}-t_{i''}|$, and then form $\hat{U}_{i'',i'}\Psi(\mathbf{r}_\perp,t_{i''})=\Psi(\mathbf{r}_\perp,t_{i'})$. This allows one to reconstruct a temporal sequence of complex wave functions, which is useful in the context of studying both nonlinear and linear wave function dynamics. This includes the topological phase dynamics associated with the nucleation and coalescence of quantized vortices [38].

B. Interference versus interferometry for nonlinear fields

The GP equation is nonlinear and therefore does not obey the superposition principle: if $\Psi_1(\mathbf{r}_\perp,t)$ and $\Psi_2(\mathbf{r}_\perp,t)$ are both solutions to Eq. (4), then $\Psi_1(\mathbf{r}_\perp,t)+\Psi_2(\mathbf{r}_\perp,t)$ will not in general be a solution. Therefore use of the term "interference" to describe the fringes of Fig. 1(a), while accurate, must not be visualized as arising from the linear superposition of two BEC wave functions that are separately valid solutions to Eq. (4). Notwithstanding this, we make the elementary remark that the concept of interference transcends the linearity assumption upon which the superposition principle is predicated.

The essence of interference is this: when two spatially separated wave functions are allowed to come into contact with one another, the square modulus of the resulting disturbance is not equal to the sum of the squared moduli of each separate disturbance. The difference between the sum of the squared moduli of each separate disturbance, and the square modulus of the resulting disturbance, is the "interference term." In this context let us consider, as an initial condition, a pair of (2+1)-dimensional wave functions $\Psi_1(\mathbf{r}_\perp,t)$ and $\Psi_2(\mathbf{r}_\perp,t)$ which are spatially separated at $t=t_0$, i.e., $\int\int|\Psi_1(\mathbf{r}_\perp,t_0)\Psi_2(\mathbf{r}_\perp,t_0)|d\mathbf{r}_\perp\approx 0$.

Linear case: If the evolution of these initially separated disturbances is governed by a linear equation, then interference effects occur if $|\Psi_1(t)|^2+|\Psi_2(t)|^2\neq|\Psi_1(t)+\Psi_2(t)|^2$ at some later time $t>t_0$. Here, $\Psi_1(t),\Psi_2(t)$, and $\Psi_1(t)+\Psi_2(t)$ are all solutions to the relevant linear equation, and functional dependence on $\mathbf{r}_\perp$ has been dropped for clarity. The associated linear interference term $I_L(t)$ is

$$\begin{aligned}I_L(t)&\equiv|\Psi_1(t)+\Psi_2(t)|^2-|\Psi_1(t)|^2-|\Psi_2(t)|^2\\&=2|\Psi_1(t)||\Psi_2(t)|\cos[\phi_1(t)-\phi_2(t)],\end{aligned} \tag{14}$$

where $\Psi_j(t)\equiv|\Psi_j(t)|\exp(i\phi_j(t))$ and $\phi_j(t)=\arg\Psi_j(t)$, with $j=1,2$. Linear interferometric phase determination aims to obtain the phase difference $\cos[\phi_1(t)-\phi_2(t)]$ from measurements of $I_L(t),|\Psi_1(t)|$, and $|\Psi_2(t)|$; typically, one of the wave phases [say, $\phi_1(t)$] is a known "reference" wave front and one seeks to determine $\phi_2(t)$.

Nonlinear case: If, instead, our initially separated disturbances are governed by a nonlinear equation, then interference effects occur when $|\Psi_1(t)|^2+|\Psi_2(t)|^2\neq|\Psi_1(t)+\Psi_2(t)+\kappa[\Psi_1(t),\Psi_2(t)]|^2$, where $\Psi_1(t),\Psi_2(t)$, and $\Psi_1(t)+\Psi_2(t)+\kappa[\Psi_1(t),\Psi_2(t)]$ are all solutions to the relevant nonlinear equation, with $\kappa[\Psi_1(t),\Psi_2(t)]$ being an appropriate interaction term which is generated when $\Psi_1(t)$ and $\Psi_2(t)$ are not spatially separated. The associated nonlinear interference term $I_{NL}(t)$ is

$$\begin{aligned}I_{NL}(t)&\equiv|\Psi_1(t)+\Psi_2(t)+\kappa[\Psi_1(t),\Psi_2(t)]|^2-|\Psi_1(t)|^2\\&\quad-|\Psi_2(t)|^2\\&=I_L(t)+2\mathrm{Re}(\kappa^*[\Psi_1(t),\Psi_2(t)][\Psi_1(t)+\Psi_2(t)])\\&\quad+|\kappa[\Psi_1(t),\Psi_2(t)]|^2,\end{aligned} \tag{15}$$

which reduces to Eq. (14) when $\kappa=0$. When $\kappa\neq 0$, Eq. (15) could, in principle, be used as a starting point for nonlinear interferometric phase determination; however, the resulting nonlinear equations are likely to be difficult to solve.

For both linear and nonlinear interferometry, the measured interference term is sensitive to the phase of the wave field, allowing one to consider the problem of inferring this phase from measurements of the wave field modulus. This is the idea behind interferogram analysis, at least for the linear case, and it is motivated by the fact that it is probability density (or intensity) rather than phase which is measured by existing detectors of high-frequency fields.

Rather than seeking an interferometric solution to the problem of phase reconstruction, the phase-retrieval viewpoint of this paper eliminates the need for a reference wave front. This can be done because the modulus of the wave field at time t is a function of both the modulus and phase of the wave field at earlier and later times. Measurement of the wave-field moduli at more than one time therefore yields information about both the modulus and phase of the wave field, without the need for interference with a reference wave.

C. Some open questions

(a) A viable approach to the phase retrieval of both linear and nonlinear multicomponent wave functions may be of utility in the study of topological structures such as skyrmions [47,48]. Can the methods of this paper be generalized to the case of multicomponent wave functions, denoted by $\{\Psi_j((\mathbf{r}_d,t))\}$, which comprise a set of K complex scalar wave functions $\Psi_j\equiv\Psi_j(\mathbf{r}_d,t), j=1,\ldots,K$, where $\mathbf{r}_d\in\mathbb{R}^d$ and $d\geqslant 2$? This $(d+1)$-dimensional multicomponent wave function might obey a system of coupled nonlinear nondissipative parabolic equations such as

$$\left(i\alpha_j\partial/\partial t+\gamma_j\nabla_d^2+\beta_j+V+\sum_{k=1}^{K} f_{kj}(|\Psi_k|)\right)\Psi_j=0, \quad (16)$$

where $\alpha_j,\beta_j,\gamma_j$ are real numbers, ∇_d^2 is the d-dimensional Laplacian, f_{kj} is a real function of a real variable, k,j are integers lying between 1 and the number K of complex scalar components Ψ_j in the multicomponent wave function, and $V\equiv V(\mathbf{r}_d,t)$ is a known real potential. In this context, the phase problem consists of reconstructing the multicomponent wave function, given the modulus of each component at a number of given times.

For a first assault on this problem, one might try

$$\{\Psi_j(\mathbf{r}_d,t_1)\} = \lim_{N\to\infty}\left(\prod_{i=1}^{M-1}\hat{P}_i\hat{U}_{i+1,i}\prod_{i=M}^{2}\hat{P}_i\hat{U}_{i-1,i}\right)^N\{|\Psi_j(\mathbf{r}_d,t_1)|\}. \quad (17)$$

Here, $\{|\Psi_j(\mathbf{r}_d,t_1)|\}$ is an array of the known moduli at $t=t_1$, which forms the initial guess for the desired multicomponent wave function $\{\Psi_j(\mathbf{r}_d,t_1)\}$. The nonlinear multicomponent time-evolution operator is defined by $\hat{U}_{m,n}\{\Psi_j(\mathbf{r}_d,t_m)\}=\{\Psi_j(\mathbf{r}_d,t_n)\}$, such that $\{\Psi_j(\mathbf{r}_d,t)\}$ is a solution to Eq. (16), and $\hat{P}_i$ is a projection operator defined by

$$\hat{P}_i\{g_j(\mathbf{r}_d,t_i)\}\equiv\{|\Psi_j(\mathbf{r}_d,t_i)|\exp(i\ \arg\ g_j(\mathbf{r}_d,t_i))\}. \quad (18)$$

Additional *a priori* knowledge may be incorporated by appropriate generalization of the method given in Sec. II, where $\hat{P}_i$ is replaced by $\hat{P}_i''\hat{P}_i$.

(b) We have restricted ourselves to the problem of phase retrieval for nondissipative nonlinear fields, for which the time-evolution operator is unitary and therefore norm preserving. If a field whether it be linear or nonlinear, obeys a *dissipative* equation—such as might be obtained by making α,β,γ,V or f complex in Eq. (4)—then the associated time-evolution operator will not be unitary. If such a nonunitary time-evolution operator is used in Eq. (5), under what circumstances will the resulting attempt at wave function reconstruction be successful? If the method is successful, how much dissipation can be tolerated before the method breaks down for a given level of noise in the data?

V. CONCLUSION

We developed and demonstrated a robust noninterferometric algorithm for reconstructing the wave function of a complex field which obeys a known $(2+1)$-dimensional nondissipative nonlinear parabolic partial differential equation, given as input data the modulus of the wave function at three or more values of the specified evolution parameter (e.g., time). As a special case of this formalism we gave a numerical study of the reconstruction of the complex macroscopic wave function associated with a $(2+1)$-dimensional Bose-Einstein condensate, given a series of absorption images as input into the algorithm. In this numerical study, the algorithm converged exponentially quickly to the noise floor imposed by the input data: the root-mean-square error of the reconstructed wave function was in all cases similar to the RMS error in the input data. The presence of both strong nonlinearities and quantized vortices was seen to increase the rate of convergence of the algorithm. The algorithm opens up the possibility of recovering a movie of the time-dependent macroscopic wave function of a BEC, and thus elucidating the phase dynamics of the condensate under experimental conditions. This includes situations where the wave function possesses topological defects. The method is also applicable to a number of other nonlinear complex wave fields, such as those encountered in paraxial nonlinear optics using both radiation and matter waves.

ACKNOWLEDGMENTS

Y-R.E.T. acknowledges financial support from the J.L. William Bequest. D.M.P. acknowledges financial support from the Australian Research Council. We acknowledge useful conversations with Yvette Hancock.

[1] S.F. Gull and G.J. Daniell, Nature (London) **272**, 686 (1978).
[2] H.A. Hauptman, Z. Kristallogr. **217**, 406 (2002).
[3] A. Barty, K.A. Nugent, D. Paganin, and A. Roberts, Opt. Lett. **23**, 817 (1998).
[4] S. Bajt, A. Barty, K.A. Nugent, M. McCartney, M. Wall, and D. Paganin, Ultramicroscopy **83**, 67 (2000).
[5] J. Miao, P. Charalambous, J. Kirz, and D. Sayre, Nature (London) **400**, 342 (1999).
[6] D.K. Saldin, R.J. Harder, V.L. Shneerson, and W. Moritz, J. Phys.: Condens. Matter **13**, 10 689 (2001).
[7] N.N. Akhmediev and A. Ankiewicz, *Solitons, Nonlinear Pulses and Beams* (Chapman and Hall, London, 1997).
[8] L. Debnath, *Nonlinear Water Waves* (Academic Press, Boston, 1994).
[9] R.T. Beyer, *Nonlinear Acoustics*, revised ed. (US Naval Ship Systems Command, Washington, 1974).
[10] W. Horton and Y-H. Ichikawa, *Chaos and Structures in Nonlinear Plasmas* (World Scientific, Singapore, 1996).
[11] E.P. Gross, Nuovo Cimento **20**, 454 (1961).
[12] E.P. Gross, J. Math. Phys. **4**, 195 (1963).
[13] L.P. Pitaevskii, Zh. Éksp. Teor. Fiz. **40**, 646 (1961) [Sov. Phys. JETP **13**, 451 (1961)].
[14] P.J. Bardroff, U. Leonhardt, and W.P. Schleich, Opt. Commun. **147**, 121 (1998).
[15] D. Paganin and K.A. Nugent, Opt. Lett. **27**, 622 (2002).
[16] M. Born and E. Wolf, *Principles of Optics*, 6th corrected ed. (Pergamon Press, Oxford, 1993).
[17] R.W. Gerchberg and W.O. Saxton, Optik (Stuttgart) **35**, 237 (1972).
[18] D. Gabor, Nature (London) **161**, 777 (1948).
[19] W.O. Saxton, *Computer Techniques for Image Processing in Electron Microscopy* (Academic Press, New York, 1978).
[20] W. Pauli, in *Handbuch der Physik*, edited by H. Geiger and K. Scheel (Springer, Berlin, 1933).
[21] J.R. Fienup, Appl. Opt. **2l**, 2758 (1982).
[22] U. Weierstall, Q. Chen, J.C.H. Spence, M.R. Howells, M. Isaacson, and R.R. Panepucci, Ultramicroscopy **90**, 171 (2002).
[23] R.W. Gerchberg and W.O. Saxton, in *Image Processing and Computer-aided Design in Electron Optics*, edited by P.W. Hawkes (Academic Press, London, 1973), p. 66.
[24] F. Gori in *Current Trends in Optics*, edited by J.C. Dainty (Academic Press, London, 1994).
[25] D.L. Misell, J. Phys. D **6**, 2200 (1973).
[26] P. Schiske, in *Image Processing and Computer-Aided Design in Electron Optics*, edited by P.W. Hawkes (Academic Press, London, 1973), p. 82.
[27] L.J. Allen, H.M.L. Faulkner, M.P. Oxley, and D. Paganin, Ultramicroscopy **88**, 85 (2001).
[28] L.J. Allen, H.M.L. Faulkner, K.A. Nugent, M.P. Oxley, and D. Paganin, Phys. Rev. E **63**, 037602 (2001).
[29] A. Papoulis, *Scattering and Diffraction in Physical Optics* (R.E. Krieger, FL, 1981).
[30] L.J. Allen, M.P. Oxley, and D. Paganin, Phys. Rev. Lett. **87**, 123902 (2001).
[31] Y.S. Kivshar and B. Luther-Davies, Phys. Rep. **298**, 81 (1998).
[32] H. Michinel, J. Campo-Táboas, R. García-Fernández, J.R. Salgueiro, and M.L. Quiroga-Teixeiro, Phys. Rev. E **65**, 066604 (2002).
[33] M.H. Anderson, J.R. Ensher, M.R. Matthews, C.E. Wieman, and E.A. Cornell, Science **269**, 198 (1995).
[34] J.R. Anglin and W. Ketterle, Nature (London) **416**, 211 (2002).
[35] M.R. Matthews, B.P. Anderson, P.C. Haljan, D.S. Hall, C.E. Wieman, and E.A. Cornell, Phys. Rev. Lett. **83**, 2498 (1999).
[36] K.W. Madison, F. Chevy, W. Wohlleben, and J. Dalibard, Phys. Rev. Lett. **84**, 806 (2000).
[37] L.D. Turner, K.P. Weber, D. Paganin, and R.E. Scholten, Opt. Lett. (to be published).
[38] L.M. Pismen, *Vortices in Nonlinear Fields: From Liquid Crystal to Superfluids, From Non-Equilibrium Patterns to Cosmic Strings* (Oxford University Press, Oxford, 1999).
[39] W. Ketterle, D.S. Durfee, and D.M. Stamper-Kurn, in *Bose-Einstein Condensation in Atomic Gases, Proceedings of the International School of Physics "Enrico Fermi," Course CXL*, edited by M. Inguscio, S. Stringari, and C.E. Wieman (IOS Press, Amsterdam, 1999), p. 67.
[40] F. Dalfovo, S. Giorgini, L.P. Pitaevskii, and S. Stringari, Rev. Mod. Phys. **71**, 463 (1999).
[41] Y. Castin and R. Dum, Eur. Phys. J. D **7**, 399 (1999).
[42] M.R. Andrews, C.G. Townsend, H.J. Miesner, D.S. Durfee, D.M. Kurn, and W. Ketterle, Science **275**, 637 (1997).
[43] B. Jackson, J.F. McCann, and C.S. Adams, Phys. Rev. Lett. **80**, 3903 (1998).
[44] S. Inouye, S. Gupta, T. Rosenband, A.P. Chikkatur, A. Gorlitz, T.L. Gustavson, A.E. Leanhardt, D.E. Pritchard, and W. Ketterle, Phys. Rev. Lett. **87**, 080402 (2001).
[45] J. Denschlag, J.E. Simsarian, D.L. Feder, C.W. Clark, L.A. Collins, J. Cubizolles, L. Deng, E.W. Hagley, K. Helmerson, W.P. Reinhardt, S.L. Rolston, B.I. Schneider, and W.D. Phillips, Science **287**, 97 (2000).
[46] J.L. McCauley, *Chaos, Dynamics and Fractals: An Algorithmic Approach to Deterministic Chaos* (Cambridge University Press, Cambridge, 1993), Chap. 1.
[47] J. Ruostekoski and J.R. Anglin, Phys. Rev. Lett. **86**, 3934 (2001).
[48] U. Al Khawaja and H. Stoof, Nature (London) **411**, 918 (2001).